Inverse Scattering of a Dielectric Sphere Partially Buried in a Ground Plane Using a Radial Basis Function Network

C. Loo and M. Hamid
University of South Alabama, Department of Electrical Engineering
Mobile, Alabama, 36688, U.S.A.
e-mail: mhamid@usouthal.edu

ABSTRACT

An analytic solution of the problem of electromagnetic scattering by a dielectric spherical scatterer resting on, or partially buried in, an infinite perfectly conducting ground plane is approximated by partially truncated sphere and is formulated using the method of images. The scattered field coefficients are solved exactly so that the scattered field can be evaluated everywhere. In particular, the scattering cross section can be calculated as a function of the sphere radius and permittivity as well as the truncated sphere distance for any specified angle of incidence. The solution of this problem is relevant to analyze the scattering by complex three-dimensional bodies, plastic mines, icebergs, rough surfaces, etc., in which the flat background can be modeled by the ground plane while the complex body can be simulated by a sphere or a system of spheres partially truncated and resting on the ground plane. In order to solve the inverse scattering problem, we employ a radial basis function network to take the scattered field complex coefficients for the TE and TM polarization case as the network inputs to predict the three outputs of the electrical radius, burial distance, and relative permittivity of the sphere. The trained network is able to retrieve the three aforementioned parameters from new data which is different from the learning data.

1. INTRODUCTION

The solution to the problem of electromagnetic inverse scattering by a partially buried dielectric sphere in an infinite plane is relevant to analyze the scattering by complex three-dimensional bodies, plastic mines, icebergs, rough surfaces, etc., in which the flat background can be modeled by the ground plane and the complex body can be simulated by a sphere or a system of spheres partially buried in the ground plane. Generally, in these applications, the detection of the dielectric characterization of the target needs to be performed directly "on field". Therefore, the development of an accurate and also fast numerical algorithm for these inverse scattering problems is essential. Analytical and numerical techniques of solving the inverse scattering problem are computationally intensive as they require matrix inversion, recurrence relations or graphical inversion methods [2-4]. In the past few years, neural network technique has been used for solving inverse scattering problems with respect to overcoming the drawback of directly solving the inverse problem [5-8]. This technique is simple, straightforward and allows a sensible reduction in the computational time and, consequently, it permits to obtain very fast solutions. This is an interesting property for all those problems requiring an analysis performed directly "on field".

The problem of forward electromagnetic scattering by a partially buried dielectric sphere in an infinite plane using truncated sphere as an approximation has been solved by Hamid and Hamid [1] (depicted in Figure 1). They solved the problem but did not carry out their solution to the same extent as reported here. The rigorous analytic solution of the problem is formulated using the method of images. The incident wave is assumed a uniform plane electromagnetic wave of arbitrary angle of incidence. The method of images is applied to replace the partially buried sphere in a ground plane by two overlapping spheres of equal size, or by two touching spheres of equal size, if the sphere is resting on the ground plane. And a supplementary incident plane electromagnetic wave is added such that the total electric field is satisfied at all points where the ground plane is located in the original problem. The incident, supplementary and scattered fields are expressed in terms of appropriate spherical wave functions. To impose the boundary conditions on the surfaces of the spheres, the translational addition theorem for the spherical wave functions is used to express the coordinate system of the scattered field from one sphere in terms of the coordinate system of the other sphere leading to a matrix equation, which can be inverted numerically to recover the scattered field coefficients.

In this paper, we improved the solution to the aforementioned scattering problem by employing the re-derived vector translational addition coefficients functions by Xu, which are quite similar to Cruzan's formula, in order to overcome the problem associate with Cruzan's formula in producing zero value for TE case [10]. The scattered field coefficients generated by exact methods are obtained, from which the scattered field can be evaluated everywhere. In particular, the scattering cross section can be calculated as a function of the sphere radius and permittivity as well as the burial distance for any specified angle of incidence.

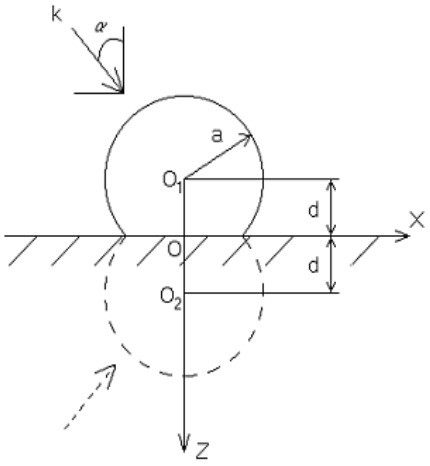

Fig. 1. Geometry of the problem.

Numerical results are presented for the normalized scattering cross-section, σ, as a function of incident angle.

In order to solve the inverse scattering of a partially truncated dielectric sphere resting on an infinite conducting plane problem, a technique based on neural network analysis is presented where the network is trained to model the nonlinear relationship between the characterization of the sphere and the complex scattering coefficients. We employ a radial basis function network that consists of an input layer with four sets of inputs, a hidden layer using Gaussian nonlinearity functions, and an output layer with three outputs. The four sets of inputs in the input layer are the real and imaginary values of the computed scattered field complex coefficients for the TE and TM polarization cases, while the outputs are the electrical radius and burial distance of the training sphere, as well as its relative permittivity. The simplified version of the network diagram is shown in Fig. 2. This network is then trained, using the orthogonal least-squares algorithm [9] with a specified range of the electrical radius (0.01λ to 5λ) and a specified number of learning data samples (50 for each output) in order to retrieve the radius, burial distance and relative permittivity of the test sphere for new data that is different from the learning data. The results are verified by applying the technique to a different set of coefficients for a wide range of dielectric constants. Typical results are presented which show excellent prediction by the neural network. The formulation to the solution of the scattering problem is given in the following section and its far field solution is given in Section 3. Details of the proposed approach of inverse scattering using neural network is explained in Section 4 follows by the description of the network training algorithm in Section 5. The computer simulation results are given in Section 6 and the conclusion is drawn in Section 7.

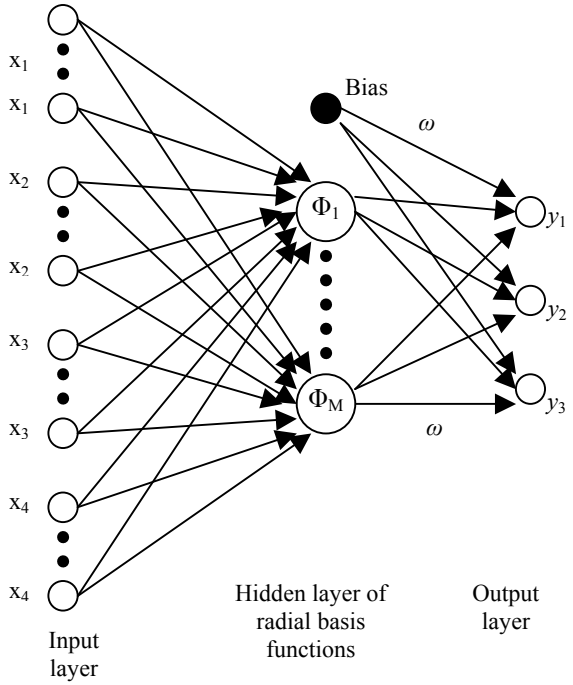

Fig. 2. Radial basis function network.

2. FORMULATION OF THE PROBLEM

Consider a dielectric spherical scatterer with radius a and relative dielectric constant ε_r to be residing on or partially truncated at an arbitrary depth d from the ground plane lying in the x-y plane. The sphere centered at O_1 is illuminated by a plane electromagnetic wave with a unit electric-field intensity whose propagation vector $\vec{k}$ lies in the x-z plane and makes an angle α with the z-axis counter-clockwise in the x-z plane as shown in Fig. 1. Thus, the incident electric and magnetic fields have the form

$$\vec{E}_i = E_0 e^{j\vec{k}\bullet\vec{r}}\hat{y} \tag{1}$$

$$\vec{H}_i = -\frac{1}{\eta}E_0 e^{j\vec{k}\bullet\vec{r}}(\cos\alpha\hat{x} - \sin\alpha\hat{z}) \tag{2}$$

where, $\vec{k} = k\sin\alpha\hat{x} + k\cos\alpha\hat{z}$ with k being the wave number, η the medium intrinsic impedance of the sphere while $\hat{x}$, $\hat{y}$, and $\hat{z}$ are the unit vectors along the x, y and z axes, respectively.

Applying the image technique with respect to the ground plane will reduce the problem to that of scattering by the sphere and its image due to the original incident wave as well as its image impinging simultaneously upon the two spheres. Using a prime superscript to denote the electric field $\vec{E}_i'$ of unit amplitude and the magnetic field $\vec{H}_i'$ of the latter image of the incident wave, we have

$$\vec{E}_i' = -E_0 e^{j\vec{k}'\bullet\vec{r}}\hat{y}$$

$$\vec{H}_i' = -\frac{1}{\eta}E_0 e^{j\vec{k}'\bullet\vec{r}}(\cos\alpha\hat{x} + \sin\alpha\hat{z})$$

where $\vec{k}' = k\sin(\pi-\alpha)\hat{x} + k\cos(\pi-\alpha)\hat{z}$

The incident plane wave can be expressed with reference to the spherical coordinate system of the sphere center O_1 as:

$$e^{jkr\cos\alpha} = \sum_{n=0}^{\infty}\sum_{m=-n}^{m=n} j^n (2n+1)\frac{(n-m)!}{(n+m)!} P_n^m(\cos\alpha) P_n^m(\cos\theta) j_n(kr) e^{jm\phi} \tag{3}$$

where P_n^m is the associated Legendre function of the first kind while j_n is the spherical Bessel function of the first kind.

Expressing the incident wave in the form of spherical wave expansion (SWE) based on scalar spherical wave mode coefficients (SSWMC) and vector spherical wave functions (VSWF), the fields due to the incident wave on the sphere are:

$$\vec{E}_i(r_1,\theta_1,\phi_1) = \sum_{n=1}^{\infty}\sum_{m=-n}^{m=n}\begin{bmatrix} P_1(m,n)\vec{N}_{mn}^{(1)}(r_1,\theta_1,\phi_1) \\ + Q_1(m,n)\vec{M}_{mn}^{(1)}(r_1,\theta_1,\phi_1)\end{bmatrix} \tag{4}$$

$$\eta\vec{H}_i(r_1,\theta_1,\phi_1) = j\sum_{n=1}^{\infty}\sum_{m=-n}^{m=n}\begin{bmatrix} P_1(m,n)\vec{M}_{mn}^{(1)}(r_1,\theta_1,\phi_1) \\ + Q_1(m,n)\vec{N}_{mn}^{(1)}(r_1,\theta_1,\phi_1)\end{bmatrix}. \tag{5}$$

The fields due to the image of the incident wave on the sphere are:

$$\vec{E}_i^{'}(r_1,\theta_1,\phi_1) = \sum_{n=1}^{\infty}\sum_{m=-n}^{m=n}\begin{bmatrix} P_2(m,n)\vec{N}_{mn}^{(1)}(r_1,\theta_1,\phi_1) \\ + Q_2(m,n)\vec{M}_{mn}^{(1)}(r_1,\theta_1,\phi_1)\end{bmatrix} \tag{6}$$

$$\eta\vec{H}_i^{'}(r_1,\theta_1,\phi_1) = j\sum_{n=1}^{\infty}\sum_{m=-n}^{m=n}\begin{bmatrix} P_2(m,n)\vec{M}_{mn}^{(1)}(r_1,\theta_1,\phi_1) \\ + Q_2(m,n)\vec{N}_{mn}^{(1)}(r_1,\theta_1,\phi_1)\end{bmatrix}. \tag{7}$$

The fields due to the incident wave on the image sphere are:

$$\vec{E}_i(r_2,\theta_2,\phi_2) = \sum_{n=1}^{\infty}\sum_{m=-n}^{m=n}\begin{bmatrix} P_3(m,n)\vec{N}_{mn}^{(1)}(r_2,\theta_2,\phi_2) \\ + Q_3(m,n)\vec{M}_{mn}^{(1)}(r_2,\theta_2,\phi_2)\end{bmatrix} \tag{8}$$

$$\eta\vec{H}_i(r_2,\theta_2,\phi_2) = j\sum_{n=1}^{\infty}\sum_{m=-n}^{m=n}\begin{bmatrix} P_3(m,n)\vec{M}_{mn}^{(1)}(r_2,\theta_2,\phi_2) \\ + Q_3(m,n)\vec{N}_{mn}^{(1)}(r_2,\theta_2,\phi_2)\end{bmatrix}. \tag{9}$$

The fields due to the image of incident wave on image sphere are:

$$\vec{E}_i^{'}(r_2,\theta_2,\phi_2) = \sum_{n=1}^{\infty}\sum_{m=-n}^{m=n}\begin{bmatrix} P_4(m,n)\vec{N}_{mn}^{(1)}(r_2,\theta_2,\phi_2) \\ + Q_4(m,n)\vec{M}_{mn}^{(1)}(r_2,\theta_2,\phi_2)\end{bmatrix} \tag{10}$$

$$\eta\vec{H}_i^{'}(r_2,\theta_2,\phi_2) = j\sum_{n=1}^{\infty}\sum_{m=-n}^{m=n}\begin{bmatrix} P_4(m,n)\vec{M}_{mn}^{(1)}(r_2,\theta_2,\phi_2) \\ + Q_4(m,n)\vec{N}_{mn}^{(1)}(r_2,\theta_2,\phi_2)\end{bmatrix}. \tag{11}$$

where $\vec{M}_{mn}^{(1)}$ and $\vec{N}_{mn}^{(1)}$ are the spherical vector wave functions of the first kind defined in terms of the spherical Bessel functions given as:

$$M_{mn} = \begin{bmatrix} \frac{m}{\sin\theta} z_n(kR) P_n^m(\cos\theta)\hat{\theta} \\ - z_n(kR)\frac{\partial}{\partial\theta} P_n^m(\cos\theta)\hat{\phi}\end{bmatrix} e^{im\phi} \tag{12}$$

$$N_{mn} = \begin{bmatrix} \frac{n(n+1)}{kR} z_n(kR) P_n^m(\cos\theta)\hat{r} \\ + \frac{1}{kR}\frac{\partial}{\partial R}\left[R z_n(kR)\right]\frac{\partial}{\partial\theta} P_n^m(\cos\theta)\hat{\theta} \\ + \frac{m}{kR\sin\theta}\frac{\partial}{\partial R}\left[R z_n(kR)\right] P_n^m(\cos\theta)\hat{\phi}\end{bmatrix} e^{im\phi} \tag{13}$$

for $M_{mn}^{(1)}$ and $N_{mn}^{(1)}$, $z_n(kR) = j_n(kR)$,

for $M_{mn}^{(3)}$ and $N_{mn}^{(3)}$, $z_n(kR) = h_n^{(1)}(kR)$,

while $P(m,n)$ and $Q(m,n)$ are known incident field coefficients for an arbitrary angle of incidence and may be written in the form:

$$P(m,n) = -j^n \frac{(2n+1)(n-m)!m}{n(n+1)(n+m)!\sin\alpha} P_n^m(\cos\alpha) \tag{14}$$

$$Q(m,n) = -j^n \frac{(2n+1)(n-m)!}{n(n+1)(n+m)!} \times \frac{\partial}{\partial\alpha} P_n^m(\cos\alpha) \tag{15}$$

$$P_1(m,n) = e^{jkd\cos\alpha} P(m,n) \tag{16}$$

$$Q_1(m,n) = e^{jkd\cos\alpha} P(m,n) \tag{17}$$

$$P_2(m,n) = (-1)^{(m+n)} e^{-jkd\cos\alpha} P(m,n) \tag{18}$$

$$Q_2(m,n) = (-1)^{(m+n)} e^{-jkd\cos\alpha} Q(m,n) \tag{19}$$

$$P_3(m,n) = e^{-jkd\cos\alpha} P(m,n) \tag{20}$$

$$Q_3(m,n) = e^{-jkd\cos\alpha} Q(m,n) \tag{21}$$

$$P_4(m,n) = (-1)^{(m+n)} e^{jkd\cos\alpha} P(m,n) \tag{22}$$

$$Q_4(m,n) = (-1)^{(m+n)} e^{jkd\cos\alpha} Q(m,n). \tag{23}$$

The scattered fields from the dielectric sphere are:

$$\vec{E}_s(r_1,\theta_1,\phi_1) = \sum_{n=1}^{\infty}\sum_{m=-n}^{m=n}\begin{bmatrix} A_E^s(m,n)\vec{N}_{mn}^{(3)}(r_1,\theta_1,\phi_1) \\ + A_M^s(m,n)\vec{M}_{mn}^{(3)}(r_1,\theta_1,\phi_1)\end{bmatrix} \tag{24}$$

$$\eta\vec{H}_s(r_1,\theta_1,\phi_1) = j\sum_{n=1}^{\infty}\sum_{m=-n}^{m=n}\begin{bmatrix} A_E^s(m,n)\vec{M}_{mn}^{(3)}(r_1,\theta_1,\phi_1) \\ + A_M^s(m,n)\vec{N}_{mn}^{(3)}(r_1,\theta_1,\phi_1)\end{bmatrix}. \tag{25}$$

The scattered fields from the image sphere are:

$$\vec{E}_s^{'}(r_2,\theta_2,\phi_2) = \sum_{n=1}^{\infty}\sum_{m=-n}^{m=n}\begin{bmatrix} B_E^s(m,n)\vec{N}_{mn}^{(3)}(r_2,\theta_2,\phi_2) \\ + B_M^s(m,n)\vec{M}_{mn}^{(3)}(r_2,\theta_2,\phi_2)\end{bmatrix} \tag{26}$$

$$\eta\vec{H}_s^{'}(r_2,\theta_2,\phi_2) = j\sum_{n=1}^{\infty}\sum_{m=-n}^{m=n}\begin{bmatrix} B_E^s(m,n)\vec{M}_{mn}^{(3)}(r_2,\theta_2,\phi_2) \\ + B_M^s(m,n)\vec{N}_{mn}^{(3)}(r_2,\theta_2,\phi_2)\end{bmatrix}. \tag{27}$$

The transmitted fields in the dielectric sphere are:

$$\vec{E}_t(r_1,\theta_1,\phi_1) = \sum_{n=1}^{\infty}\sum_{m=-n}^{m=n}\begin{bmatrix} A_E^t(m,n)\vec{N}_{mn}^{(1)}(r_1,\theta_1,\phi_1) \\ + A_M^t(m,n)\vec{M}_{mn}^{(1)}(r_1,\theta_1,\phi_1)\end{bmatrix} \tag{28}$$

$$\eta\vec{H}_t(r_1,\theta_1,\phi_1) = j\sum_{n=1}^{\infty}\sum_{m=-n}^{m=n}\begin{bmatrix} A_E^t(m,n)\vec{M}_{mn}^{(1)}(r_1,\theta_1,\phi_1) \\ + A_M^t(m,n)\vec{N}_{mn}^{(1)}(r_1,\theta_1,\phi_1)\end{bmatrix}. \tag{29}$$

The transmitted fields in the image sphere are:

$$\vec{E}_t^{'}(r_2,\theta_2,\phi_2) = \sum_{n=1}^{\infty}\sum_{m=-n}^{m=n}\begin{bmatrix} B_E^t(m,n)\vec{N}_{mn}^{(1)}(r_2,\theta_2,\phi_2) \\ + B_M^t(m,n)\vec{M}_{mn}^{(1)}(r_2,\theta_2,\phi_2)\end{bmatrix} \tag{30}$$

$$\eta\vec{H}_t^{'}(r_2,\theta_2,\phi_2) = j\sum_{n=1}^{\infty}\sum_{m=-n}^{m=n}\begin{bmatrix} B_E^t(m,n)\vec{M}_{mn}^{(1)}(r_2,\theta_2,\phi_2) \\ + B_M^t(m,n)\vec{N}_{mn}^{(1)}(r_2,\theta_2,\phi_2)\end{bmatrix}. \tag{31}$$

Note that in the transmitted fields, k is replaced by k_2. $k_2 = \sqrt{\varepsilon_r}k$, if the dielectric sphere is a perfect dielectric with no magnetic losses. To impose the boundary condition at $r_1 = a$, the outgoing scattered fields from the image sphere must be expressed in terms of incoming fields to the real sphere and vice versa, hence we apply the spherical vector translational addition theorem, i. e.

$$\vec{M}_{mn}^{(3)}(r_2,\theta_2,\phi_2) = \sum_{v=1}^{\infty}\sum_{\mu=-v}^{\mu=v}\begin{bmatrix} A_{\mu\nu}^{mn}(d_{12},\theta_{12},\phi_{12})\vec{M}_{\mu\nu}^{(1)}(r_1,\theta_1,\phi_1) \\ + B_{\mu\nu}^{mn}(d_{12},\theta_{12},\phi_{12})\vec{N}_{\mu\nu}^{(1)}(r_1,\theta_1,\phi_1)\end{bmatrix} \tag{32}$$

$$\vec{N}_{mn}^{(3)}(r_2,\theta_2,\phi_2) = \sum_{v=1}^{\infty}\sum_{\mu=-v}^{\mu=v}\begin{bmatrix} A_{\mu\nu}^{mn}(d_{12},\theta_{12},\phi_{12})\vec{N}_{\mu\nu}^{(1)}(r_1,\theta_1,\phi_1) \\ + B_{\mu\nu}^{mn}(d_{12},\theta_{12},\phi_{12})\vec{M}_{\mu\nu}^{(1)}(r_1,\theta_1,\phi_1)\end{bmatrix} \tag{33}$$

$$\vec{M}_{mn}^{(3)}(r_1,\theta_1,\phi_1)=\sum_{v=1}^{\infty}\sum_{\mu=-v}^{\mu=v}(-1)^{n+v}\begin{bmatrix}A_{\mu v}^{mn}(d_{21},\theta_{21},\phi_{21})\vec{M}_{\mu v}^{(1)}(r_2,\theta_2,\phi_2)\\+B_{\mu v}^{mn}(d_{21},\theta_{21},\phi_{21})\vec{N}_{\mu v}^{(1)}(r_2,\theta_2,\phi_2)\end{bmatrix} \tag{34}$$

$$\vec{N}_{mn}^{(3)}(r_1,\theta_1,\phi_1)=\sum_{v=1}^{\infty}\sum_{\mu=-v}^{\mu=v}(-1)^{n+v}\begin{bmatrix}A_{\mu v}^{mn}(d_{21},\theta_{21},\phi_{21})\vec{N}_{\mu v}^{(1)}(r_2,\theta_2,\phi_2)\\+B_{\mu v}^{mn}(d_{21},\theta_{21},\phi_{21})\vec{M}_{\mu v}^{(1)}(r_2,\theta_2,\phi_2)\end{bmatrix}. \tag{35}$$

where $A_{\mu v}^{mn}$ and $A_{\mu v}^{mn}$ are Xu's translation addition theorem coefficients given in the Appendix and

$$d_{12}=d_{21}=\sqrt{(x_2-x_1)^2+(y_2-y_1)^2+(z_2-z_1)^2}$$

$$\theta_{12}=\cos^{-1}\left(\frac{z_2-z_1}{d_{12}}\right),\quad \theta_{21}=\cos^{-1}\left(\frac{z_1-z_2}{d_{21}}\right)$$

$$\phi_{12}=\tan^{-1}\left(\frac{y_2-y_1}{x_2-x_1}\right),\quad \phi_{21}=\tan^{-1}\left(\frac{y_1-y_2}{x_1-x_2}\right).$$

In our case, since the image sphere is always positioned below the real sphere on the conducting ground, θ_{12}, θ_{21}, ϕ_{12}, and ϕ_{21} are equal to zero and $d_{12}=-d_{21}=2d$. The boundary condition on the surface of the dielectric sphere and its image requires continuity of the tangential electric and magnetic field. Hence,

$$\hat{r}_1\times\begin{bmatrix}\vec{E}_i(a,\theta_1,\phi_1)+\vec{E}_i^{'}(a,\theta_1,\phi_1)\\+\vec{E}_s(a,\theta_1,\phi_1)+\vec{E}_s^{'}(a^*,\theta_1^*,\phi_1^*)\end{bmatrix}=\hat{r}_1\times\vec{E}_t(a,\theta_1,\phi_1) \tag{36}$$

$$\hat{r}_1\times\frac{1}{\eta_1}\begin{bmatrix}\vec{H}_i(a,\theta_1,\phi_1)+\vec{H}_i^{'}(a,\theta_1,\phi_1)\\+\vec{H}_s(a,\theta_1,\phi_1)+\vec{H}_s^{'}(a^*,\theta_1^*,\phi_1^*)\end{bmatrix}=\hat{r}_1\times\frac{1}{\eta_2}\vec{H}_t(a,\theta_1,\phi_1) \tag{37}$$

$$\hat{r}_2\times\begin{bmatrix}\vec{E}_i(a,\theta_2,\phi_2)+\vec{E}_i^{'}(a,\theta_2,\phi_2)\\+\vec{E}_s^{'}(a,\theta_2,\phi_2)+\vec{E}_s(a^*,\theta_2^*,\phi_2^*)\end{bmatrix}=\hat{r}_2\times\vec{E}_t^{'}(a,\theta_2,\phi_2) \tag{38}$$

$$\hat{r}_2\times\frac{1}{\eta_1}\begin{bmatrix}\vec{H}_i(a,\theta_2,\phi_2)+\vec{H}_i^{'}(a,\theta_2,\phi_2)\\+\vec{H}_s^{'}(a,\theta_2,\phi_2)+\vec{H}_s(a^*,\theta_2^*,\phi_2^*)\end{bmatrix}=\hat{r}_2\times\frac{1}{\eta_2}\vec{H}_t^{'}(a,\theta_2,\phi_2) \tag{39}$$

where $\hat{r}_1$ and $\hat{r}_2$ are the outward unit normal to the surface of the dielectric sphere and its image, respectively. From the boundary condition above, the electric and magnetic fields on the surface of the sphere and its image can be expressed as:

$$\vec{E}^{Total}(a,\theta,\phi)=\vec{E}_i(a,\theta,\phi)+\vec{E}_i^{'}(a,\theta,\phi)+\vec{E}_s(a,\theta,\phi)+\vec{E}_s^{'}(a,\theta',\phi') \tag{40}$$

$$\vec{H}^{Total}(a,\theta,\phi)=\vec{H}_i(a,\theta,\phi)+\vec{H}_i^{'}(a,\theta,\phi)+\vec{H}_s(a,\theta,\phi)+\vec{H}_s^{'}(a,\theta',\phi') \tag{41}$$

and

$$\vec{E}^{Total}(a,\theta',\phi')=\vec{E}_i(a,\theta',\phi')+\vec{E}_i^{'}(a,\theta',\phi')+\vec{E}_s(a,\theta,\phi)+\vec{E}_s^{'}(a,\theta',\phi') \tag{42}$$

$$\vec{H}^{Total}(a,\theta',\phi')=\vec{H}_i(a,\theta',\phi')+\vec{H}_i^{'}(a,\theta',\phi')+\vec{H}_s(a,\theta,\phi)+\vec{H}_s^{'}(a,\theta',\phi'). \tag{43}$$

From the boundary condition 1, we have:

$$\hat{r}_1\times\sum_{n=1}^{\infty}\sum_{m=-n}^{m=n}\begin{bmatrix}\left\{P_1(m,n)\vec{N}_{mn}^{(1)}(a,\theta_1,\phi_1)+Q_1(m,n)\vec{M}_{mn}^{(1)}(a,\theta_1,\phi_1)\right\}\\+\left\{P_2(m,n)\vec{N}_{mn}^{(1)}(a,\theta_1,\phi_1)+Q_2(m,n)\vec{M}_{mn}^{(1)}(a,\theta_1,\phi_1)\right\}\\+\left\{A_E^s(m,n)\vec{N}_{mn}^{(3)}(a,\theta_1,\phi_1)+A_M^s(m,n)\vec{M}_{mn}^{(3)}(a,\theta_1,\phi_1)\right\}+\\\left\{\begin{bmatrix}B_E^s(m,n)\sum_{v=1}^{\infty}\sum_{\mu=-v}^{\mu=v}\begin{bmatrix}A_{\mu v}^{mn}(d_{12},\theta_{12},\phi_{12})\vec{N}_{\mu v}^{(1)}(a,\theta_1,\phi_1)\\+B_{\mu v}^{mn}(d_{12},\theta_{12},\phi_{12})\vec{M}_{\mu v}^{(1)}(a,\theta_1,\phi_1)\end{bmatrix}\\+B_M^s(m,n)\sum_{v=1}^{\infty}\sum_{\mu=-v}^{\mu=v}\begin{bmatrix}A_{\mu v}^{mn}(d_{12},\theta_{12},\phi_{12})\vec{M}_{\mu v}^{(1)}(a,\theta_1,\phi_1)\\+B_{\mu v}^{mn}(d_{12},\theta_{12},\phi_{12})\vec{N}_{\mu v}^{(1)}(a,\theta_1,\phi_1)\end{bmatrix}\end{bmatrix}\right\}\end{bmatrix}$$

$$=\hat{r}_1\times\sum_{n=1}^{\infty}\sum_{m=-n}^{m=n}\left[A_E^t(m,n)\vec{N}_{mn}^{(1)}(a,\theta_1,\phi_1)+A_M^t(m,n)\vec{M}_{mn}^{(1)}(a,\theta_1,\phi_1)\right] \tag{44}$$

From the boundary condition 2, we have:

$$\hat{r}_1\times\frac{1}{\eta_1}\sum_{n=1}^{\infty}\sum_{m=-n}^{m=n}\begin{bmatrix}\left\{P_1(m,n)\vec{M}_{mn}^{(1)}(a,\theta_1,\phi_1)+Q_1(m,n)\vec{N}_{mn}^{(1)}(a,\theta_1,\phi_1)\right\}\\+\left\{P_2(m,n)\vec{M}_{mn}^{(1)}(a,\theta_1,\phi_1)+Q_2(m,n)\vec{N}_{mn}^{(1)}(a,\theta_1,\phi_1)\right\}\\+\left\{A_E^s(m,n)\vec{M}_{mn}^{(3)}(a,\theta_1,\phi_1)+A_M^s(m,n)\vec{N}_{mn}^{(3)}(a,\theta_1,\phi_1)\right\}+\\\left\{\begin{bmatrix}B_E^s(m,n)\sum_{v=1}^{\infty}\sum_{\mu=-v}^{\mu=v}\begin{bmatrix}A_{\mu v}^{mn}(d_{12},\theta_{12},\phi_{12})\vec{M}_{\mu v}^{(1)}(a,\theta_1,\phi_1)\\+B_{\mu v}^{mn}(d_{12},\theta_{12},\phi_{12})\vec{N}_{\mu v}^{(1)}(a,\theta_1,\phi_1)\end{bmatrix}\\+B_M^s(m,n)\sum_{v=1}^{\infty}\sum_{\mu=-v}^{\mu=v}\begin{bmatrix}A_{\mu v}^{mn}(d_{12},\theta_{12},\phi_{12})\vec{N}_{\mu v}^{(1)}(a,\theta_1,\phi_1)\\+B_{\mu v}^{mn}(d_{12},\theta_{12},\phi_{12})\vec{M}_{\mu v}^{(1)}(a,\theta_1,\phi_1)\end{bmatrix}\end{bmatrix}\right\}\end{bmatrix}$$

$$=\hat{r}_1\times\frac{1}{\eta_2}\sum_{n=1}^{\infty}\sum_{m=-n}^{m=n}\left[A_E^t(m,n)\vec{M}_{mn}^{(1)}(a,\theta_1,\phi_1)+A_M^t(m,n)\vec{N}_{mn}^{(1)}(a,\theta_1,\phi_1)\right] \tag{45}$$

From the boundary condition 3, we have:

$$\hat{r}_2\times\sum_{n=1}^{\infty}\sum_{m=-n}^{m=n}\begin{bmatrix}\left\{P_3(m,n)\vec{N}_{mn}^{(1)}(a,\theta_2,\phi_2)+Q_3(m,n)\vec{M}_{mn}^{(1)}(a,\theta_2,\phi_2)\right\}\\+\left\{P_4(m,n)\vec{N}_{mn}^{(1)}(a,\theta_2,\phi_2)+Q_4(m,n)\vec{M}_{mn}^{(1)}(a,\theta_2,\phi_2)\right\}\\+\left\{B_E^s(m,n)\vec{N}_{mn}^{(3)}(a,\theta_2,\phi_2)+B_M^s(m,n)\vec{M}_{mn}^{(3)}(a,\theta_2,\phi_2)\right\}+\\\left\{\begin{bmatrix}A_E^s(m,n)\sum_{v=1}^{\infty}\sum_{\mu=-v}^{\mu=v}(-1)^{n+v}\begin{bmatrix}A_{\mu v}^{mn}(d_{21},\theta_{21},\phi_{21})\vec{N}_{\mu v}^{(1)}(a,\theta_2,\phi_2)\\+B_{\mu v}^{mn}(d_{21},\theta_{21},\phi_{21})\vec{M}_{\mu v}^{(1)}(a,\theta_2,\phi_2)\end{bmatrix}\\+A_M^s(m,n)\sum_{v=1}^{\infty}\sum_{\mu=-v}^{\mu=v}(-1)^{n+v}\begin{bmatrix}A_{\mu v}^{mn}(d_{21},\theta_{21},\phi_{21})\vec{M}_{\mu v}^{(1)}(a,\theta_2,\phi_2)\\+B_{\mu v}^{mn}(d_{21},\theta_{21},\phi_{21})\vec{N}_{\mu v}^{(1)}(a,\theta_2,\phi_2)\end{bmatrix}\end{bmatrix}\right\}\end{bmatrix}$$

$$=\hat{r}_2\times\sum_{n=1}^{\infty}\sum_{m=-n}^{m=n}\left[B_E^t(m,n)\vec{N}_{mn}^{(1)}(a,\theta_2,\phi_2)+B_M^t(m,n)\vec{M}_{mn}^{(1)}(a,\theta_2,\phi_2)\right] \tag{46}$$

From the boundary condition 4, we have:

$$\hat{r}_2\times\frac{1}{\eta_1}\sum_{n=1}^{\infty}\sum_{m=-n}^{m=n}\begin{bmatrix}\left\{P_3(m,n)\vec{M}_{mn}^{(1)}(a,\theta_2,\phi_2)+Q_3(m,n)\vec{N}_{mn}^{(1)}(a,\theta_2,\phi_2)\right\}\\+\left\{P_4(m,n)\vec{M}_{mn}^{(1)}(a,\theta_2,\phi_2)+Q_4(m,n)\vec{N}_{mn}^{(1)}(a,\theta_2,\phi_2)\right\}\\+\left\{B_E^s(m,n)\vec{M}_{mn}^{(3)}(a,\theta_2,\phi_2)+B_M^s(m,n)\vec{N}_{mn}^{(3)}(a,\theta_2,\phi_2)\right\}+\\\left\{\begin{bmatrix}A_E^s(m,n)\sum_{v=1}^{\infty}\sum_{\mu=-v}^{\mu=v}(-1)^{n+v}\begin{bmatrix}A_{\mu v}^{mn}(d_{21},\theta_{21},\phi_{21})\vec{M}_{\mu v}^{(1)}(a,\theta_2,\phi_2)\\+B_{\mu v}^{mn}(d_{21},\theta_{21},\phi_{21})\vec{N}_{\mu v}^{(1)}(a,\theta_2,\phi_2)\end{bmatrix}\\+A_M^s(m,n)\sum_{v=1}^{\infty}\sum_{\mu=-v}^{\mu=v}(-1)^{n+v}\begin{bmatrix}A_{\mu v}^{mn}(d_{21},\theta_{21},\phi_{21})\vec{N}_{\mu v}^{(1)}(a,\theta_2,\phi_2)\\+B_{\mu v}^{mn}(d_{21},\theta_{21},\phi_{21})\vec{M}_{\mu v}^{(1)}(a,\theta_2,\phi_2)\end{bmatrix}\end{bmatrix}\right\}\end{bmatrix}$$

$$=\hat{r}_2\times\frac{1}{\eta_2}\sum_{n=1}^{\infty}\sum_{m=-n}^{m=n}\begin{bmatrix}B_E^t(m,n)\vec{M}_{mn}^{(1)}(a,\theta_2,\phi_2)\\+B_M^t(m,n)\vec{N}_{mn}^{(1)}(a,\theta_2,\phi_2)\end{bmatrix}. \tag{47}$$

Applying the orthogonality properties of the spherical wave functions yields the solution for the scattered field coefficients

$$A_E^S(m,n)=\upsilon_n(\alpha)\left\{\begin{bmatrix}P_1(m,n)+P_2(m,n)\end{bmatrix}+\sum_{v=1}^{\infty}\sum_{\mu=-v}^{v}\begin{bmatrix}A_{\mu v}^{mn}(d_{12},\theta_{12},\phi_{12})B_E^S(\mu,v)\\+B_{\mu v}^{mn}(d_{12},\theta_{12},\phi_{12})B_M^S(\mu,v)\end{bmatrix}\right\} \tag{48}$$

$$A_M^S(m,n)=u_n(\alpha)\left\{\begin{bmatrix}Q_1(m,n)+Q_2(m,n)\end{bmatrix}+\sum_{v=1}^{\infty}\sum_{\mu=-v}^{v}\begin{bmatrix}A_{\mu v}^{mn}(d_{12},\theta_{12},\phi_{12})B_M^S(\mu,v)\\+B_{\mu v}^{mn}(d_{12},\theta_{12},\phi_{12})B_E^S(\mu,v)\end{bmatrix}\right\} \tag{49}$$

$$B_E^S(m,n)=\upsilon_n(\alpha)\left\{\begin{bmatrix}P_3(m,n)+P_4(m,n)+\end{bmatrix}\sum_{v=1}^{\infty}\sum_{\mu=-v}^{v}(-1)^{n+v}\begin{bmatrix}A_{\mu v}^{mn}(d_{21},\theta_{21},\phi_{21})A_E^S(\mu,v)\\+B_{\mu v}^{mn}(d_{21},\theta_{21},\phi_{21})A_M^S(\mu,v)\end{bmatrix}\right\} \tag{50}$$

$$B_M^S(m,n)=u_n(\alpha)\left\{\begin{bmatrix}Q_3(m,n)+Q_4(m,n)+\end{bmatrix}\sum_{v=1}^{\infty}\sum_{\mu=-v}^{v}(-1)^{n+v}\begin{bmatrix}A_{\mu v}^{mn}(d_{21},\theta_{21},\phi_{21})A_M^S(\mu,v)\\+B_{\mu v}^{mn}(d_{21},\theta_{21},\phi_{21})A_E^S(\mu,v)\end{bmatrix}\right\} \tag{51}$$

where $\upsilon_n(\alpha)$ and $u_n(\alpha)$ are the electric and magnetic scattering coefficients for a single dielectric sphere, which are given by

$$\upsilon_n(ka) = -\frac{j_n(\mathrm{m}ka)[ka\, j_n(ka)]' - j_n(ka)[\mathrm{m}ka\, j_n(\mathrm{m}ka)]'}{j_n(\mathrm{m}ka)[ka\, h_n^{(1)}(ka)]' - h_n^{(1)}(ka)[\mathrm{m}ka\, j_n(\mathrm{m}ka)]'} \quad (52)$$

$$u_n(ka) = -\frac{j_n(ka)[\mathrm{m}ka\, j_n(\mathrm{m}ka)]' - \mathrm{m}^2 j_n(\mathrm{m}ka)[ka\, j_n(ka)]'}{h_n^{(1)}(ka)[\mathrm{m}ka\, j_n(\mathrm{m}ka)]' - \mathrm{m}^2 j_n(\mathrm{m}ka)[ka\, h_n^{(1)}(ka)]'} \quad (53)$$

where $ka = 2\pi\, a / \lambda$ and $\mathrm{m} = k_2 / k = \sqrt{\varepsilon_2 / \varepsilon}$ is the refractive index of the dielectric, which may be real or complex depending on whether the dielectric is lossless or lossy, while ε_2 and ε are the permittivities of the sphere and the surrounding medium, respectively. Equations (48) to (51) above can be written in matrix form as

$$[A_E^S] = \upsilon_n(P_1 + P_2) + \upsilon_n[A^{12}][B_E^S] + \upsilon_n[B^{12}][B_M^S] \quad (54)$$

$$[A_M^S] = u_n(Q_1 + Q_2) + u_n[A^{12}][B_M^S] + u_n[B^{12}][B_E^S] \quad (55)$$

$$[B_E^S] = \upsilon_n(P_3 + P_4) + \upsilon_n[A^{21}][A_E^S] + \upsilon_n[B^{21}][A_M^S] \quad (56)$$

$$[B_M^S] = u_n(Q_3 + Q_4) + u_n[A^{21}][A_M^S] + u_n[B^{21}][A_E^S]. \quad (57)$$

Equations (54) to (57) are a set of complex linear algebraic equations, and should be solved simultaneously to yield the unknown scattering coefficients. The above system may be rewritten in the following form

$$\begin{bmatrix} -I & 0 & \upsilon_n[A^{12}] & \upsilon_n[B^{12}] \\ 0 & -I & u_n[B^{12}] & u_n[A^{12}] \\ \upsilon_n[A^{21}] & \upsilon_n[B^{21}] & -I & 0 \\ u_n[B^{21}] & u_n[A^{21}] & 0 & -I \end{bmatrix} \begin{bmatrix} [A_E^S] \\ [A_M^S] \\ [B_E^S] \\ [B_M^S] \end{bmatrix} = \begin{bmatrix} \upsilon_n(P_1 + P_2) \\ u_n(Q_1 + Q_2) \\ \upsilon_n(P_3 + P_4) \\ u_n(Q_3 + Q_4) \end{bmatrix} \quad (58)$$

where $[A^{12}], [A^{21}], [B^{12}]$ and $[B^{21}]$ are matrices associated with the translation addition coefficients. And $[A_E^S]$, $[A_M^S]$, $[B_E^S]$ and $[B_M^S]$ are column matrices containing the scattering coefficients. The above equation can now be solved directly by either using Cramer's rule or by multiplication of the inverse matrix of the diagonal matrix on the left side of equation (58). In addition, the infinite series must be truncated to a finite number of terms $n = \nu = \mathrm{M}$ and $m = \mu = 2\mathrm{M} + 1$. Solution of equation (58) yields the scattered coefficients in equations (24), (25), (26), and (27). For our case of θ_{pq} and ϕ_{pq} equal to zero, the above system ($\mu = m$) could be solved for each m independently, since there is no coupling between azimuthal modes. Once the scattered field coefficients are computed, the total scattered field can be determined everywhere from the expressions:

$$\vec{E}_{Total}^{S}(r_1,\theta_1,\phi_1) = \sum_{n=1}^{\infty}\sum_{m=-n}^{m=n} \begin{bmatrix} P_2(m,n)\vec{N}_{mn}^{(3)}(r_1,\theta_1,\phi_1) \\ + Q_2(m,n)\vec{M}_{mn}^{(3)}(r_1,\theta_1,\phi_1) \\ + A_E^S(m,n)\vec{N}_{mn}^{(3)}(r_1,\theta_1,\phi_1) \\ + A_M^S(m,n)\vec{M}_{mn}^{(3)}(r_1,\theta_1,\phi_1) \\ + B_E^S(m,n)\vec{N}_{mn}^{(3)}(r_2,\theta_2,\phi_2) \\ + B_M^S(m,n)\vec{M}_{mn}^{(3)}(r_2,\theta_2,\phi_2) \end{bmatrix} \quad (65)$$

$$\eta\vec{H}_{Total}^{S}(r_1,\theta_1,\phi_1) = j\sum_{n=1}^{\infty}\sum_{m=-n}^{m=n} \begin{bmatrix} P_2(m,n)\vec{M}_{mn}^{(3)}(r_1,\theta_1,\phi_1) \\ + Q_2(m,n)\vec{N}_{mn}^{(3)}(r_1,\theta_1,\phi_1) \\ + A_E^S(m,n)\vec{M}_{mn}^{(3)}(r_1,\theta_1,\phi_1) \\ + A_M^S(m,n)\vec{N}_{mn}^{(3)}(r_1,\theta_1,\phi_1) \\ + B_E^S(m,n)\vec{M}_{mn}^{(3)}(r_2,\theta_2,\phi_2) \\ + B_M^S(m,n)\vec{N}_{mn}^{(3)}(r_2,\theta_2,\phi_2) \end{bmatrix}. \quad (66)$$

3. FAR-FIELD APPROXIMATIONS

As shown in the previous section, both of the individual scattered fields from component spheres are solved in respective sphere-centered coordinate systems. Following the solution of boundary conditions for all partial scattering coefficients, the next step is to construct a single-field representation for the total scattered field from an aggregate of two spheres as a whole. This step is important for navigating towards a complete two-sphere scattering solution. Of particular interest are the far zone scattered fields. In the far field approximation ($kr_1 \gg 1$, and $kr_2 \gg 1$) we have,

$$r_1 = r + d\cos\theta \quad , \quad r_2 = r - d\cos\theta \quad (67)$$

$$\theta \approx \theta_1 \approx \theta_2 \quad (68)$$

$$h_n^{(1)}(kr_1) \approx (-j)^{(n+1)}\frac{e^{jkr_1}}{kr_1} \quad , \quad h_n^{(1)}(kr_2) \approx (-j)^{(n+1)}\frac{e^{jkr_2}}{kr_2} \quad (69)$$

$$\frac{[kr_1 h_n^{(1)}(kr_1)]'}{kr_1} \approx (-j)^n\frac{e^{jkr_1}}{kr_1} \quad , \quad \frac{[kr_2 h_n^{(1)}(kr_2)]'}{kr_2} \approx (-j)^n\frac{e^{jkr_2}}{kr_2}. \quad (70)$$

Referring to a common coordinate centered at O as shown in Fig. 1, the total scattered field can also be expanded in VSWF with a very simple transformation involving only a simple phase term. This is because the translation of VSWF between displaced coordinate systems has an obviously correct asymptotic form valid in the far zone:

$$M_{mn}^{(3)}(r_1,\theta_1,\phi_1) = e^{jkd\cos\theta}M_{mn}^{(3)}(r,\theta,\phi) \quad , r \to \infty \quad (71)$$

$$N_{mn}^{(3)}(r_1,\theta_1,\phi_1) = e^{jkd\cos\theta}N_{mn}^{(3)}(r,\theta,\phi) \quad , r \to \infty \quad (72)$$

$$M_{mn}^{(3)}(r_2,\theta_2,\phi_2) = e^{-jkd\cos\theta}M_{mn}^{(3)}(r,\theta,\phi) \quad , r \to \infty \quad (73)$$

$$N_{mn}^{(3)}(r_2,\theta_2,\phi_2) = e^{-jkd\cos\theta}N_{mn}^{(3)}(r,\theta,\phi) \quad , r \to \infty. \quad (74)$$

Substituting the above equations into equations (24) and (26), and summing both equations together yields the total scattered electric field in the far zone.

$$E_{Total}^{S} = \frac{e^{jkr}}{kr}\left\{\begin{matrix}\left[F_{\theta 1}(\theta,\phi) + F_{\theta 2}(\theta,\phi) + F_{\theta 3}(\theta,\phi)\right]\hat{\theta} \\ + \left[F_{\phi 1}(\theta,\phi) + F_{\phi 2}(\theta,\phi) + F_{\phi 3}(\theta,\phi)\right]\hat{\phi}\end{matrix}\right\} \quad (75)$$

where

$$F_{\theta 1}(\theta,\phi) = \sum_{n=1}^{\infty}\sum_{m=-n}^{n} j^{-n+1}\begin{bmatrix} -P(m,n)\dfrac{\partial}{\partial\theta}P_n^m(\cos\theta) \\ + Q(m,n)\dfrac{m}{\sin\theta}P_n^m(\cos\theta)\end{bmatrix}\cos m\phi \quad (76)$$

$$F_{\phi 1}(\theta,\phi) = \sum_{n=1}^{\infty}\sum_{m=-n}^{n} j^{-n+1}\begin{bmatrix} P(m,n)\dfrac{m}{\sin\theta}P_n^m(\cos\theta) \\ + Q(m,n)\dfrac{\partial}{\partial\theta}P_n^m(\cos\theta)\end{bmatrix}\sin m\phi \quad (77)$$

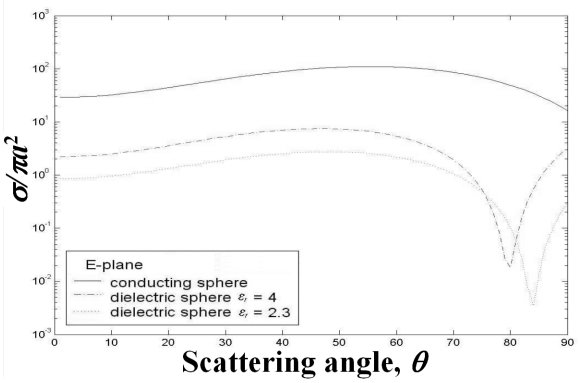

Fig. 3. Normalized bistatic cross-sections in the E plane of a partially buried dielectric sphere vs. the scattering angle θ for $ka = 1.0$, $d = a$, and $\varepsilon_r = \infty$, 4, 2.3.

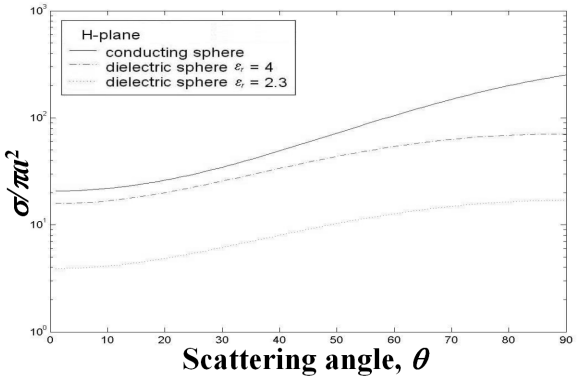

Fig. 4. Normalized bistatic cross-sections in the H plane of a partially buried dielectric sphere vs. the scattering angle θ for $ka = 1.0$, $d = a$, and $\varepsilon_r = \infty$, 4, 2.3.

$$F_{\theta 2}(\theta,\phi)=\sum_{n=1}^{\infty}\sum_{m=-n}^{n} j^{-n+1}\begin{bmatrix} -A_E^S(m,n)\dfrac{\partial}{\partial\theta}P_n^m(\cos\theta) \\ +A_M^S(m,n)\dfrac{m}{\sin\theta}P_n^m(\cos\theta)\end{bmatrix}\cos m\phi\, e^{jkd\cos\theta} \tag{78}$$

$$F_{\phi 2}(\theta,\phi)=\sum_{n=1}^{\infty}\sum_{m=-n}^{n} j^{-n+1}\begin{bmatrix} A_E^S(m,n)\dfrac{m}{\sin\theta}P_n^m(\cos\theta) \\ +A_M^S(m,n)\dfrac{\partial}{\partial\theta}P_n^m(\cos\theta)\end{bmatrix}\sin m\phi\, e^{jkd\cos\theta} \tag{79}$$

$$F_{\theta 3}(\theta,\phi)=\sum_{n=1}^{\infty}\sum_{m=-n}^{n} j^{-n+1}\begin{bmatrix} -B_E^S(m,n)\dfrac{\partial}{\partial\theta}P_n^m(\cos\theta) \\ +B_M^S(m,n)\dfrac{m}{\sin\theta}P_n^m(\cos\theta)\end{bmatrix}\cos m\phi\, e^{-jkd\cos\theta} \tag{80}$$

$$F_{\phi 3}(\theta,\phi)=\sum_{n=1}^{\infty}\sum_{m=-n}^{n} j^{-n+1}\begin{bmatrix} B_E^S(m,n)\dfrac{m}{\sin\theta}P_n^m(\cos\theta) \\ +B_M^S(m,n)\dfrac{\partial}{\partial\theta}P_n^m(\cos\theta)\end{bmatrix}\sin m\phi\, e^{-jkd\cos\theta}. \tag{81}$$

Often the scattered radiation is most conveniently measured by the bistatic radar cross-section. The bistatic radar cross-section is defined as

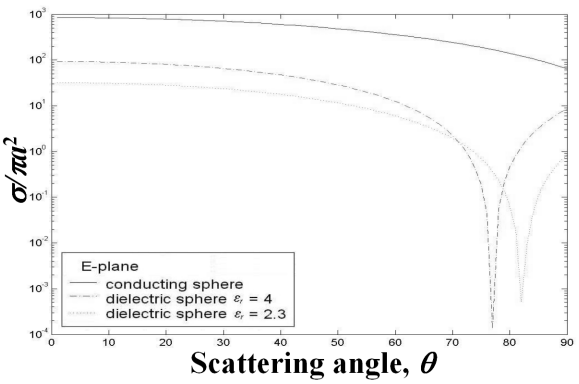

Fig. 5. Normalized bistatic cross-sections in the E plane of a partially buried dielectric sphere vs. the scattering angle θ for $ka = 1.0$, $d = 0.5a$, and $\varepsilon_r = \infty$, 4, 2.3.

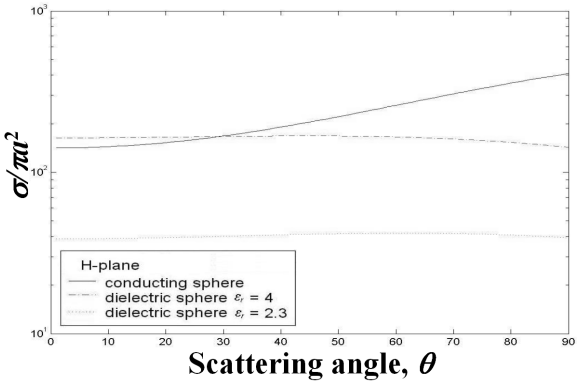

Fig. 6. Normalized bistatic cross-sections in the H plane of a partially buried dielectric sphere vs. the scattering angle θ for $ka = 1.0$, $d = 0.5a$, and $\varepsilon_r = \infty$, 4, 2.3.

$$\sigma(\theta,\phi)=\lim_{r\to\infty}4\pi r^2\left|E_{Total}^S\cdot\hat{\tau}\right|^2\Big/\left|E_i\right|^2 \tag{82}$$

with the unit vector $\hat{\tau}$ denoting the direction of polarization of the receiver at the observation point. When $\hat{\tau}$ has the same direction as E_{Total}^S, the normalized bistatic radar cross-section is given by

$$\frac{\sigma(\theta,\phi)}{\pi a^2}=\frac{4}{(ka)^2}\left[\begin{matrix}\left|F_{\theta 1}(\theta,\phi)+F_{\theta 2}(\theta,\phi)+F_{\theta 3}(\theta,\phi)\right|^2 \\ +\left|F_{\phi 1}(\theta,\phi)+F_{\phi 2}(\theta,\phi)+F_{\phi 3}(\theta,\phi)\right|^2\end{matrix}\right]. \tag{83}$$

The normalized bistatic radar cross-sections in the E and H planes are obtained by substituting $\phi=\pi/2$ and $\phi=0$, respectively, into Eq. (83). For the back-scattering cross-section, when $\theta=\pi-\alpha$ and $\phi=\pi$, the corresponding normalized back-scattering cross section is

$$\frac{\sigma(\alpha)}{\pi a^2}=\frac{4}{(ka)^2}\left|F_{\phi 1}(\theta,\phi)+F_{\phi 2}(\theta,\phi)+F_{\phi 3}(\theta,\phi)\right|^2. \tag{84}$$

The normalized bistatic cross-section patterns in the E and H planes are plotted for the partially buried dielectric sphere versus the scattering angle θ, taken between 0º and 90º, and corresponding to end fire incidence ($\alpha = 0^\circ$), as well as for different burial

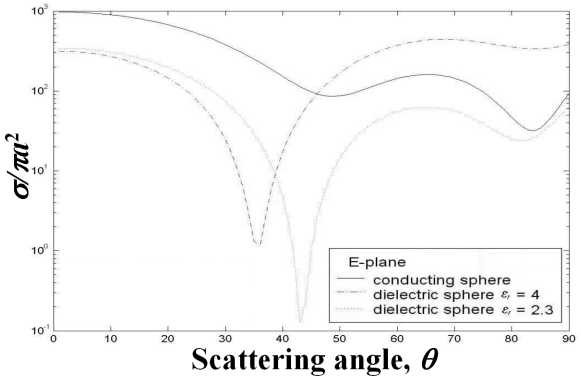

Fig. 7. Normalized bistatic cross-section in the E plane of a partially buried dielectric sphere vs. the scattering angle θ for $ka = 2.0$, $d = 0.75a$, and $\varepsilon_r = \infty$, 4, 2.3.

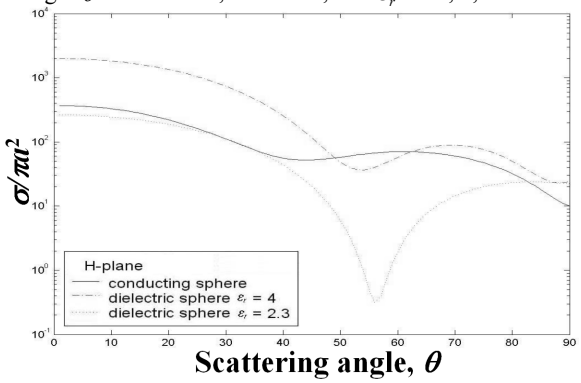

Fig. 8. Normalized bistatic cross-section in the H plane of a partially buried dielectric sphere vs. the scattering angle θ for $ka = 2.0$, $d = 0.75a$, and $\varepsilon_r = \infty$, 4, 2.3.

distances. Figures 3 and 4 show the normalized scattering cross-sections for a sphere of electrical radius ka = 1.0, burial distance $d = a$, and relative dielectric constant ε_r = 4 and ε_r = 2.3. Furthermore, Figures 3 and 4 compare the numerical results of the conducting sphere residing on the ground plane that is represented by a continuous-line curve with the dielectric spheres with relative permittivity $\varepsilon_r = 4$ and $\varepsilon_r = 2.3$ represented by the broken-line curve and dotted-line curves, respectively. The three curves have almost the same behavior except for a resonance that occurs at θ = 79° and 84° for the non-conducting spheres in the E plane. It can also be seen that the magnitude of the backscattering cross section for the dielectric cases are lower in average for both planes. Figures 5 and 6 show the normalized bistatic cross-sections of the same electrical radius and relative dielectric constants but with a burial distance of $d = 0.5a$. It appears that the dielectric spheres now show much significant resonance behavior at $\theta = 78°$ and 82°. Figures 7 to 10 show the normalized bistatic cross-sections for a partially buried sphere of electrical radius ka = 2.0 with the same relative dielectric constants but with a burial distance of

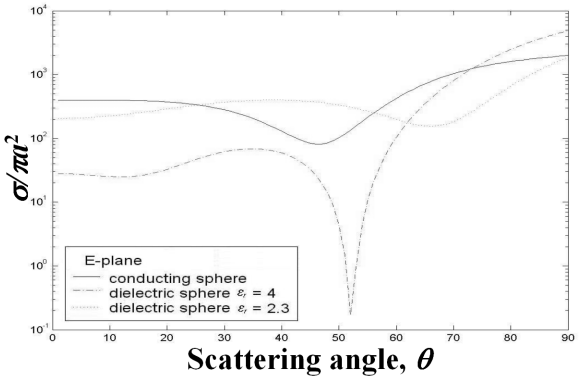

Fig. 9. Normalized bistatic cross-section in the E plane of a partially buried dielectric sphere vs. the scattering angle θ for $ka = 2.0$, $d = 0.5a$, and $\varepsilon_r = \infty$, 4, 2.3.

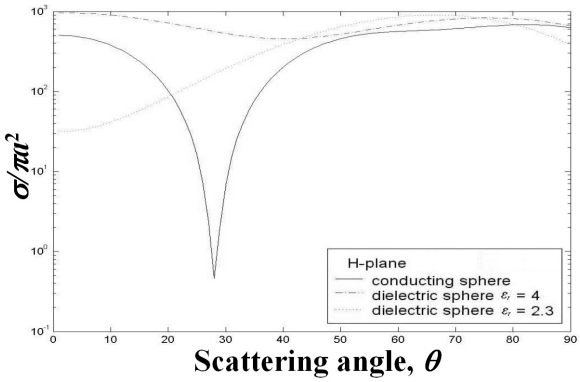

Fig. 10. Normalized bistatic cross-section in the H plane of a partially buried dielectric sphere vs. the scattering angle θ for $ka = 2.0$, $d = 0.5a$, and $\varepsilon_r = \infty$, 4, 2.3.

$d = 0.7a$, and $d = 0.5a$, respectively. It can be seen that the behavior of the curves has become wavier as electrical radius of the sphere is increased.

4. THE NEURAL NETWORK APPROACH

Radial basis functions (RBF) emerged as a variant of artificial neural network in the late 1980's. However, their roots are entrenched in much older pattern recognition techniques as, for example, potential functions, clustering, functional approximation, spline interpolation and mixture models. Their excellent approximation capabilities have been studied by Park and Sandbeg [11], and Poggio and Girosi [12]. Due to their nonlinear approximation properties, RBF networks are able to model complex mappings, which perception neural networks can only model by means of multiple intermediary layers.

In order to estimate the relative permittivity ε_r, the electrical radius and the burial distance of the sphere, a/λ and d/λ of the sphere, respectively, we employ the radial basis function network shown schematically in Fig. 2. The network consists of three

layers; an input layer that consists of four sets of inputs, a hidden layer using Gaussian nonlinearity functions, and an output layer with three outputs. Each hidden unit represents a single radial basis function, with associated center position and width. Such hidden units are sometimes referred to as centroids or kernels. Each output unit performs a weighted summation of the hidden units, using the $\omega_j s$ as weights. The four sets of inputs in the input layer are the real and imaginary values of the computed scattered field complex coefficients for the TE ($A_E^S \& B_E^S$) and TM ($A_M^S \& B_M^S$) polarization cases, while the outputs are the electrical radius and burial distance of the sphere as well as its relative permittivity. This network is designed to perform nonlinear mapping from the input layer to the hidden layer, which is then followed by linear mapping from the hidden layer to the output layer. For this, we choose a function $y_k(\mathrm{x})$ with the following form:

$$y_k(\mathrm{x}) = \sum_{j=1}^{M} \omega_{kj} \phi\left(\left\| x - \mu_j \right\|\right) \tag{85}$$

variable x represents the input vector while $\phi(\|...\|)$ are nonlinear functions known as the radial basis functions that consist of Gaussian function $\phi_c(r) = e^{-r^2/\sigma^2}$ and Euclidean norm ||...||. The known data points, μ_j, are taken to be the centers of the radial basis functions. The design of the network includes the selection of the width parameter σ_j and the weighting functions ω_j such that it minimizes the difference between the network output and the desired output. The training of the network will be discussed in the next section followed by the demonstration of the training results in Section 6.

5. NETWORK TRAINING

In order to use a Radial Basis Function Network, we need to specify the hidden unit activation function, the number of processing units, a criterion for modeling a given task and a training algorithm for finding the parameters of the network. Finding the three sets of RBF network parameters (the centers, the widths, and the weights) is called network training. There are two categories of training algorithms: supervised and unsupervised. RBF networks are used mainly in supervised applications. In a supervised application, we are provided with an asset of data samples called a training set for which the corresponding network outputs are known. In this case, the network parameters are found such that they minimize a cost function:

$$\min \sum_{k=1}^{M} \left\{ t_k^n - y_k(x^n) \right\}^2 \tag{86}$$

where M is the total number of vectors from the training set, t_k^n is the target value of the output vector and $y_k(x^n)$ represents the output vector associated with a data sample x^n from the training set. If Gaussian basis functions are used to minimize this cost function, one can perform a stochastic gradient descent and readily obtain the update equations:

$$\Delta\omega_{kj} = \eta_1 (t_k^n - y_k(x^n)) \phi_j(x^n) \tag{87}$$

$$\Delta\mu_j = \eta_2 \phi_j(x^n) \frac{\left\| x^n - \mu_j \right\|}{\sigma_j^2} \sum_{k=1}^{M} \left\{ y_k\left(t_k^n\right) - x^n \right\} \omega_{kj} \tag{88}$$

$$\Delta\sigma_j = \eta_3 \phi_j(x^n) \frac{\left\| x^n - \mu_j \right\|^2}{\sigma_j^3} \sum_{k=1}^{M} \left\{ y_k\left(t_k^n\right) - x^n \right\} \omega_{kj} \tag{89}$$

where η_1, η_2, η_3 are the learning rates.

In unsupervised training, the output assignment is not available for the given training set. One of the approaches is assigning a basis function for each of the data samples. This solution proved to be expensive in terms of memory requirement and in the number of parameters. Other approaches choose randomly, or assume known, the hidden unit weights and calculate the output weights ω_{jk} by solving a system of equations whose solution is given in the training set. The matrix inversion required in this approach is computationally expensive and could cause numerical problems in certain situations (when the matrix is singular).

For RBF networks, finding the right number of free parameters is crucial. This involves trying to determine the optimal number of hidden units. Hence, the analysis of the effect of adding a new hidden unit or removing an existing unit is an important one. Backward elimination and forward selection are two ways of pruning and growing RBF networks. In backward elimination, a network is constructed with all the basic functions in the candidate pool. At each step, the unit that least increases the error is eliminated from the network. Again, this procedure is continued until some model selection criterion stops decreasing. At this point, the complexity of the model is assumed sufficient to represent the underlying function complexity.

In forward selection, one is given an initial network configuration and a candidate pool of basis functions; typically Gaussians centered at the training data points. At each step, the hidden basis function unit, which decreases the error most, such as sum-squared-error, is removed from the candidate pool and added to the network. Though forward selection is a nonlinear optimization technique, it has the advantages of not having to fix the number of hidden units in advance, tractable model selection criteria, and computational efficiency. The projection matrix for the case where an extra hidden unit has been added is given by

$$P_{m+1} = P_m - \frac{P_m f_J f_J^T P_m}{f_J^T P_m f_J} \tag{90}$$

where, f_J is the column of the design matrix, Φ, corresponding to the most recently recruited hidden

unit. The reduction in the sum-squared-error due to the addition of the unit is given by

$$\hat{S}_m - \hat{S}_{m+1} = \frac{(\hat{y}P_m f_J)^2}{f_J^T P_m f_J}. \quad (91)$$

The unit, which reduces the sum-squared-error most, is the chosen candidate. Geometrically, this will be the unit whose corresponding basis vector is most closely aligned to the perpendicular from $\hat{y}$ to the current m-dimensional space. Though the sum-squared-error reduces as more hidden units are added, the model selection criterion will reach a minimum before it starts increasing again. This is the point where the process is stopped.

Forward selection is a relatively fast algorithm but it can be speeded up even further using a technique called orthogonal least squares [9]. This is a Gram-Schmidt orthogonalization process [15], which ensures that each new column added to the design matrix of the growing subset is orthogonal to all previous columns. This simplifies the equation for the change in sum-squared-error and results in a more efficient algorithm.

Any matrix can be factored into the product of a matrix with orthogonal columns and a matrix which is upper triangular. In particular, the design matrix, $H_m \in \Re^{p\times m}$, can be factored into

$$H_m = \widetilde{H}_m U_m \quad (92)$$

where $\widetilde{H}_m = \left[\widetilde{h}_1 \;\; \widetilde{h}_2 \;\; \cdots \;\; \widetilde{h}_m\right] \in \Re^{p\times m}$ has orthogonal columns $\left(\widetilde{h}_{1i}^T \widetilde{h}_j = 0, i \neq j\right)$ and $U_m \in \Re^{m\times m}$ is upper triangular.

When considering whether to add the basis function corresponding to *J*-th column, $\widetilde{f}_J$ of the full design matrix, the projection of $\widetilde{f}_J$ in the space already spanned by the *m* columns of the current design matrix is irrelevant. Only its projection perpendicular to this space, namely

$$\widetilde{f}_J = f_J - \sum_{j=1}^{m} \frac{f_J^T \widetilde{h}_j}{\widetilde{h}_j^T \widetilde{h}_j} \widetilde{h}_j \quad (93)$$

can contribute to a further reduction in the training error, and this reduction is

$$\hat{S}_m - \hat{S}_{m+1} = \frac{(\hat{y}^T \widetilde{f}_J)^2}{\widetilde{f}_J^T \widetilde{f}_J}. \quad (94)$$

Computation of this change in sum-squared-error is lower compared to the unnormalized version given in equation (91). This is the basis of the increased efficiency of orthogonal least squares.

A small overhead is necessary to maintain the columns of the full design matrix orthogonal to the space spanned by the columns of the growing design matrix and to update the upper triangular matrix. After $\widetilde{f}_J$ is selected the new orthogonalized full design matrix is

$$\widetilde{F}_{m+1} = \widetilde{F}_m - \frac{\widetilde{f}_J \widetilde{f}_J^T \widetilde{F}_m}{\widetilde{f}_J^T \widetilde{f}_J} \quad (95)$$

and the upper triangular matrix is updated to

$$U_m = \begin{bmatrix} U_{m-1} & (\widetilde{H}_{m-1}^T \widetilde{H}_{m-1})^{-1} \widetilde{H}_{m-1}^T f_J \\ O_{m-1}^T & 1 \end{bmatrix}. \quad (96)$$

Initially $U_1 = 1$ and $\widetilde{F}_0 = F$. The orthogonalized optimal weight vector

$$\widetilde{w}_m = \left(\widetilde{H}_m^T \widetilde{H}_m\right)^{-1} H_m^T \hat{y} \quad (97)$$

and the unorthoganalized optimal weight equation are then related by

$$\hat{w}_m = U_m^{-1} \widetilde{w}_m. \quad (98)$$

6. NETWORK SIMULATION RESULTS

The training and testing of the proposed Radial Basis Function Network was carried out using MATLAB script. After the Radial Basis Function Network is trained with a set of chosen learning data, a new set of test data that is different from the learning data is generated to evaluate the trained network. The learning data set requires 50 distinct sample values for each of the three outputs. Therefore, 125,000 samples are required as the learning data set. The range of the electrical radius *a,* of the training sphere is from 0.01λ to 5λ. The range of the burial distance is from 0 to *a* (half buried in the conducting ground to residing on the surface of the conducting ground) while the range of the relative permittivity ε_r is from 1 to 9. Each of the sample sets holds 4 set of inputs and 3 target outputs. The 4 set of inputs are:

x_{1j} : Real value of scattered field coefficients for TE polarization case:

$real(A_E^S(m,n))$ and $real(B_E^S(m,n))$

x_{2j} : Real value of scattered field coefficients for TM polarization case:

$real(A_M^S(m,n))$ and $real(B_M^S(m,n))$

x_{3j} : Imaginary value of scattered field coefficients for TE polarization case:

$imag(A_E^S(m,n))$ and $imag(B_E^S(m,n))$

x_{4j} : Imaginary value of scattered field coefficients for TM polarization case:

$imag(A_M^S(m,n))$ and $imag(B_M^S(m,n))$

where j = 1,. . ., *d* and $d = 4n^2 + 2n = 42$.

The higher the order of *n*, the higher the accuracy of the outputs and the large data set of the mapping function can become very costly to evaluate. Nevertheless, the coefficients of order up to the 3rd order (*n*=3) were sufficient for training of a sphere with electric radius 0.01λ to 5λ. Similarly, the use of only one set of the scattered field coefficients ($real(A_E^S(m,n))$) will result in poor performance.

The test results are plotted in Figs. 11 to 18. Figures 11 and 12 show the RBF network estimated burial distance of the sphere with electric radius k*a* = 1

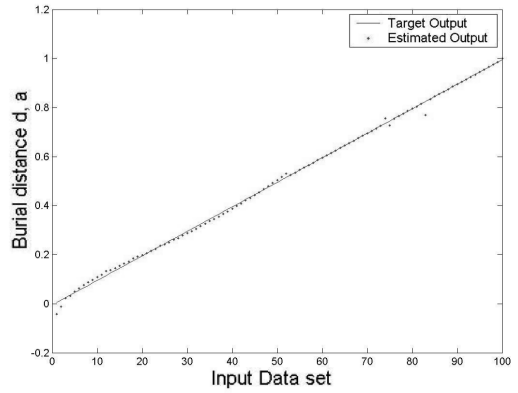

Average absolute error = 0.0043
% error relative to sphere radius = 0.43%

Fig. 11. RBF network estimated burial distance (*ka*=1.0 and $\varepsilon_r = 2.3$ (m=1.51)).

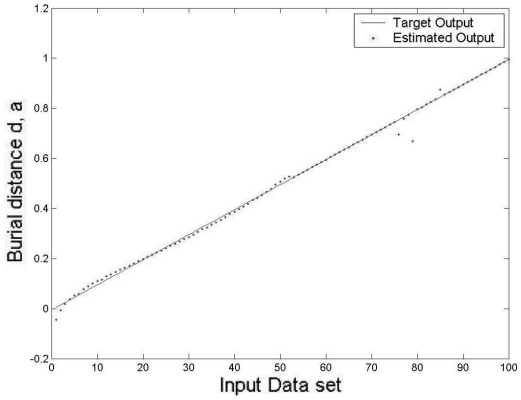

Average absolute error = 0.0067
% error relative to sphere radius = 0.67%

Fig. 12. RBF network estimated burial distance (*ka*=1.0 and ε_r=4.0 (m=2.0)).

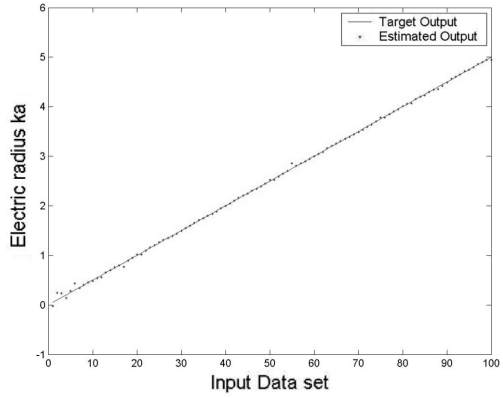

Average absolute error = 0.0159
Average relative percentage error = 4.95%

Fig. 13. RBF network estimated electric radius (d=0.5a and $\varepsilon_r = 2.3$ (m=1.51)).

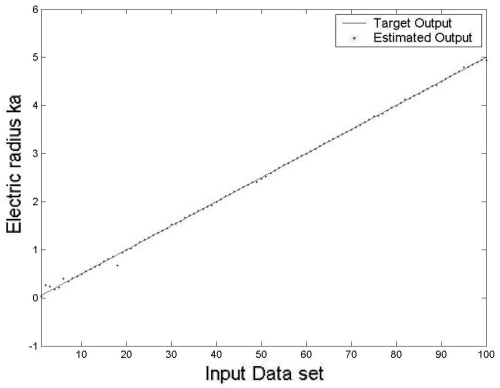

Average absolute error = 0.0144
Average relative percentage error = 3.73%

Fig. 14. RBF network estimated electric radius (*d*=0.5*a* and ε_r=4.0 (m=2.0)).

and relative permittivity, $\varepsilon_r = 2.3$, and $\varepsilon_r = 4$, respectively. When burial distance d = 0, the sphere is half buried in the conducting ground and when burial distance d = *a*, the sphere is touching and residing on the conducting ground. From the results plotted in Fig. 11 and Fig. 12, the estimated burial distance is found to be very accurate as the percentage error of the estimated burial distance relative to the sphere radius is less than 1%. Figures 13 and 14 show the RBF network estimated electric radius of the sphere with burial distance $d = 0.5a$ and relative permittivity $\varepsilon_r = 2.3$, and $\varepsilon_r = 4$, respectively. The network gives poor prediction results when the electrical radius *ka* of the sphere is below 1 and close to zero, where the sphere is disappearing. While Figures 15 to 18 show the RBF network estimated refraction index m of the sphere with electrical radius *ka* = 1 and burial distance $d = 0$, $d = 0.25a$, $d = 0.5a$, and $d = a$, respectively. As expected, the estimated sphere parameters are very close to the target values.

7. CONCLUSION

The first part of this paper describes an exact solution to the problem of scattering by a partially truncated dielectric sphere resting on a ground plane. The different bistatic cross-section results were obtained for various electrical radii, burial depths or the truncated depths and relative permittivity of the sphere. Since the medium intrinsic impedance of the sphere, η, is a function of the relative dielectric constant of the material of the sphere ε_r. It is obvious that the present solution should tend to that of a conducting sphere partially buried in a ground plane as $\varepsilon_r \to \infty$.

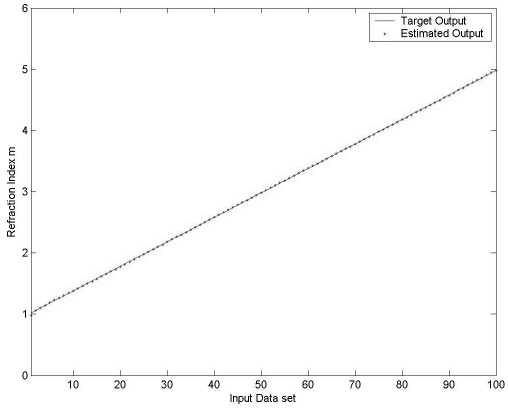

Average absolute error = 0.0038
Average relative percentage error = 0.18%

Fig. 15. RBF network estimated refraction index m (*ka*=1 and *d*=0).

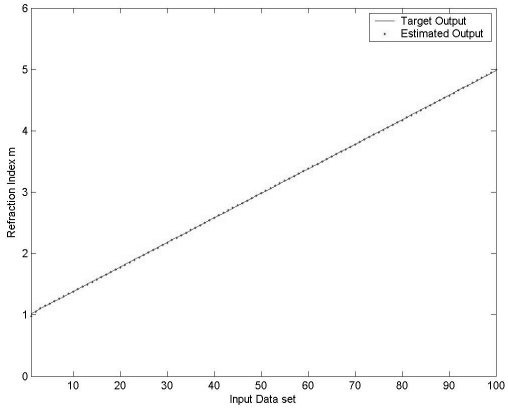

Average absolute error = 0.0038
Average relative percentage error = 0.18%

Fig. 16. RBF network estimated refraction index m (*ka*=1 and *d*=0.25*a*).

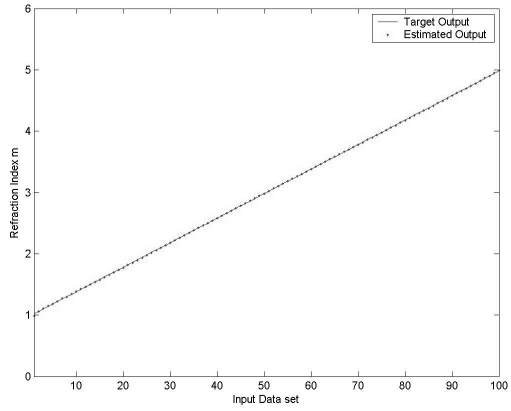

Average absolute error = 0.0036
Average relative percentage error = 0.16%

Fig. 17. RBF network estimated refraction index m (*ka*=1 and *d*=0.5*a*).

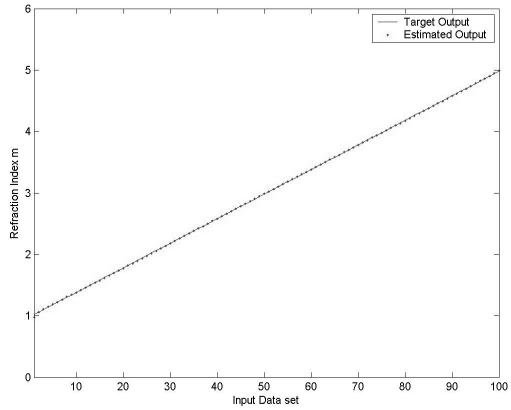

Average absolute error = 0.0037
Average relative percentage error = 0.18%

Fig. 18. RBF network estimated refraction index m (*ka*=1 and *d*=*a*).

Furthermore, the solution should tend to well known solutions for the special cases when $d \to 0$ [13,14].

Comparing to analytical and numerical techniques, the proposed method of using neural networks in inverse scattering is simple, straightforward and timesaving, since it does not require matrix inversion, recurrence relations or graphical inversion methods to retrieve the desired parameters of the sphere. From the computer simulation results, the proposed method has proven effective in predicting the non-linear relation between the scattered field coefficient inputs and the sphere parameter outputs. The network has successfully retrieved the burial distance, radius, and relative permittivity of the dielectric sphere partially buried in a conducting ground given the scattering coefficients of the scatterer. Above and beyond, the performance of the proposed RBF network is proportional to the number of learning samples. T

herefore, by increasing the number of learning samples, a better prediction of the network will be achieved.

ACKNOWLEDGEMENT

The authors wish to acknowledge the financial assistance of the National Science Foundation.

REFERENCES

[1] A.-K. Hamid, and M. Hamid, "Electromagnetic scattering by a dielectric sphere partially buried in an infinite plane," *Canadian Journal of Physics*, vol. 80, pp. 979-986, 2002.

[2] C. Eftimiu, "Direct and inverse scattering by a sphere of variable index of refraction," *Journal of Mathematical Physics*, vol. 23, no. 11, pp. 2140-2146. 1982.

[3] J. Sylvester, and D. P. Winebrenner, "Linear and nonlinear inverse scattering," *SIAM Journal of Applied Mathematics* 59(2), pp. 669-699, 1998.

[4] I. T. Rekanos, T. V. Yioultsis & T.D.Tsiboukis " Inverse scattering using the finite-element method and a nonlinear optimization Technique ", *IEEE Trans. On Microwave Theory and Techniques*, vol. 47, no. 3, pp. 336-344,1999.

[5] A-K Hamid, "A neural-network approach to the inverse-scattering problem from a circular conducting cylindrical scatterer," *Microwave and Optical Tech. Letters*, vol. 13, no. 6, pp. 380-382, 1998.

[6] E. Bermani, S. Caorsi, M. Raffetto, "An inverse scattering approach based on a neural network technique for the detection of dielectric cylinders buried in a lossy half-space," *Progress in Electromagnetics Research*, no. 26, pp. 69-90, 2000.

[7] S. Caorsi and P. Gamba, "Electromagnetic detection of dielectric cylinder by a neural network approach," *IEEE Trans. on Geoscience and Remote Sensing*, vol. 37, 820-827, 1999.

[8] X. Gong and Y. Wang, "A neural network approach to the microwave inverse scattering problem with edge-preserving regularization," *Radio Science*, vol. 36, no. 5, pp. 825-832, 2001.

[9] S. Chen, C. F. N. Cowan, and P. M. Grant. "Orthogonal least squares learning for radial basis function networks," *IEEE Trans. On Neural Networks*, vol. 2, no. 2, pp. 302-309, 1991.

[10] Y. L. Xu, "Electromagnetic scattering by an aggregate of spheres: Far field," *Appl. Optics.* vol. 36, pp. 9496-9508, 1997.

[11] J. Park and J. W. Sandbeg, "Universal approximation using radial basis functions network," *Neural Computation*, vol. 3, pp. 246-257, 1991.

[12] T. Poggio and F. Girosi, (1990) "Networks for approximation and learning," *Proc. IEEE*, vol. 78, no. 9, pp. 1481-1497.

[13] J. A. Stratton, Electromagnetic Theory, McGraw-Hill, New York, 1941.

[14] P. Bhartia, R. A. Ross and M. Hamid, "Ray optical scattering by two spheres", Arch. Elekt. Ubertrag., vol. 24, pp. 215-222, 1970.

[15] R. A. Horn and C. R. Johnson. "Matrix Analysis," *Cambridge University Press*, Cambridge, UK, 1985.

APPENDIX

Xu's vector translation addition theorem coefficients:

$$A_{\mu\nu}^{mn}(d_{pq},\theta_{pq},\phi_{pq}) = (-1)^{m+n} a_0 \frac{2n+1}{2n(n+1)} e^{j(\mu-m)\phi_{pq}} \times \sum_p \left\{ j^{p-n-v} \begin{bmatrix} n(n+1) \\ +v(v+1) \\ -p(p+1) \end{bmatrix} a_1 z_p^{(J)}(kd_{pq}) P_p^{\mu-m}\cos(\theta_{pq}) \right\} \quad \text{(A1)}$$

$$B_{\mu\nu}^{mn}(d_{pq},\theta_{pq},\phi_{pq}) = (-1)^{m+n} a_0 b_0 \frac{2n+1}{2n(n+1)} e^{j(\mu-m)\phi_{pq}} \times \sum_p \left\{ j^{p-n-v+1} \begin{bmatrix} 2(n+1)(v-\mu)a_2 \\ -\left[\begin{matrix} p(p+3)-v(v+1) \\ -n(n+3)-2\mu(n+1) \end{matrix} \right] a_3 \\ \times z_{p+1}^{(J)}(kd_{pq}) P_{p+1}^{\mu-m}\cos(\theta_{pq}) \end{bmatrix} \right\} \quad \text{(A2)}$$

where

$z_p^{(J)} = z_p^{(J)}$, if $r \le d_{pq}$

$z_p^{(J)} = j_p^{(1)}$, if $r \ge d_{pq}$

$a_0 = a(-m,n,\mu,v,n+v)$

$a_1 = \dfrac{a(-m,n,\mu,v,p)}{a(-m,n,\mu,v,n+v)}$

$a_2 = \dfrac{a(-m-1,n+1,\mu+1,v,p+1)}{a(-m-1,n+1,\mu+1,v,n+v+1)}$

$a_3 = \dfrac{a(-m,n+1,\mu,v,p+1)}{a(-m,n+1,\mu,v,n+v+1)}$

$b_0 = \dfrac{(2n+1)(n+v+m-\mu+1)}{(2n+2v+1)(n+m+1)}$

and *a(m,n,μ,v,p)* is the Gaunt coefficient given by,

$$a(m,n,\mu,,v,p) = (-1)^{m+\mu}(2p+1)\left[\frac{(n+m)!(v+\mu)!(p-m-\mu)!}{(n-m)!(v-\mu)!(p+m+\mu)!}\right]^{\frac{1}{2}} \times \begin{pmatrix} n & v & p \\ 0 & 0 & 0 \end{pmatrix} \begin{pmatrix} n & v & p \\ m & \mu & (-m-\mu) \end{pmatrix} \quad \text{(A3)}$$

where the symbol $\begin{pmatrix} j_1 & j_2 & j_3 \\ m_1 & m_2 & m_3 \end{pmatrix}$ is the so-called Wigner 3-j symbol. The integer p in the summations takes the values $n+v,\ n+v-2,\ \ldots,\ |n-v|$.

Chye-Hwa Loo received his B.S. degree in 2001, and his M.S. degree in 2003, both in Electrical Engineering from the University of South Alabama. Currently he is a Ph.D. student in the Department of Electrical Engineering at University of Mississippi. His research interests are remote sensing and scattering.

Michael Hamid Graduated from McGill University in Montreal with a B. Eng. Degree in 1960, a M. Eng. Degree in 1962 and from the University of Toronto with a Ph.D. degree in 1966, all in Electrical Engineering. He joined the University of Manitoba in 1965 where he became a Professor of Electrical Engineering and Head of the Antenna Laboratory. He was a Visiting Professor at the University of California Davis and Central Florida and is presently a Professor of Electrical Engineering at the University of South Alabama. He is a past president of the International Microwave Power Institute, a Fellow of IEE and IEEE and published 310 refereed articles and 25 patents.